GA–A22831

MONTE CARLO IMPURITY TRANSPORT MODELING IN THE DIII–D TRANSPORT

by
T.E. EVANS and D.F. FINKENTHAL

APRIL 1998

DISCLAIMER

GA–A22831

MONTE CARLO IMPURITY TRANSPORT MODELING IN THE DIII–D TRANSPORT

by
T.E. EVANS and D.F. FINKENTHAL[†]

[†]Palomar College

This is a preprint of a paper to be presented at the 11th American Physical Society Topical Conference on Atomic Processes in Plasmas, March 23–26, 1998, Auburn, Alabama and to be published in the *proceedings*.

Work supported by
the U.S. Department of Energy
under Contract No. DE-AC03-89ER51114

GA PROJECT 3466
APRIL 1998

Monte Carlo Impurity Transport Modeling in the DIII–D Tokamak

T.E. Evans* and D.F. Finkenthal†

*General Atomics, PO Box 85608, San Diego, CA 92186
†Palomar College, 1140 West Mission Road, San Marcos, CA 92069

Abstract. A description of the carbon transport and sputtering physics contained in the Monte Carlo Impurity (MCI) transport code is given. Examples of statistically significant carbon transport pathways are examined using MCI's unique tracking visualizer and a mechanism for enhanced carbon accumulation on the high field side of the divertor chamber is discussed. Comparisons between carbon emissions calculated with MCI and those measured in the DIII–D tokamak are described. Good qualitative agreement is found between 2D carbon emission patterns calculated with MCI and experimentally measured carbon patterns. While uncertainties in the sputtering physics, atomic data, and transport models have made quantitative comparisons with experiments more difficult, recent results using a physics based model for physical and chemical sputtering has yielded simulations with about 50% of the total carbon radiation measured in the divertor. These results and plans for future improvement in the physics models and atomic data are discussed.

I. INTRODUCTION

The control of non-hydrogenic core and boundary layer impurities is a critical issue for fusion energy production in magnetic confinement devices. In large magnetic fusion devices such as ITER small amounts of non-hydrogenic impurities significantly degrade the performance of the device both by diluting the DT fuel and by radiating energy from the core where high plasma temperatures are required for the efficient production of fusion power. Calculations based on the ITER design indicate that the effective charge (Z_{eff}) of the core plasma must be kept below 1.6 in order to maintain acceptable operating conditions (1). In addition, heat conduction from the core plasma into the edge requires that the radiated power exceed 80% of the total loss power to prevent target plate damage. Experiments in existing tokamaks have demonstrated that these levels of radiation can, in fact, be obtained without significantly degrading the core confinement but in some cases the core impurity concentration exceeds Z_{eff} = 1.6. DIII–D has achieved good performance using D_2 puffing to increase the radiation from D_α and intrinsic carbon impurities. Lower wall heat fluxas were achieved at Z_{eff} < 1.8. In JET it was found that by combining D_2 and N_2 gas puffs a high radiated power fraction (~85%) could be obtained in the divertor region with good core confinement. Unfortunately, the core impurity concentration increased steadily throughout these shots exceeding Z_{eff} = 2.5 over the entire high confinement phase and resulting in a steady decline in the neutron production rate (2). Thus, it is not yet

clear whether radiative divertors sustained by injecting either pure D_2 or a mixture of D_2 and a radiating impurity, are capable of providing a complete solution for particle and heat flux control. Consequently, comprehensive numerical models of the edge plasma and its interactions with plasma facing material surfaces are essential for developing a better understanding of the complex processes involved in optimizing the radiative divertor approach. The DIII–D Monte Carlo Impurity (MCI) model discussed here is one part of an array of numerical models being developed for this purpose.

II. DIVERTOR MODELING BACKGROUND

As originally envisioned, the roll of a perfect axisymmetric poloidal divertor is to move impurity sources as far as possible from the good confinement region by creating a layer where all of the magnetic field lines terminate on material surfaces buried deep inside chambers which are well isolated from the main plasma. Conceptually, the idea is that these open field lines form a so-called scrape-off layer (SOL) around the hot plasma where the flow of background deuterium ions (D^+), which have escaped the main plasma, drag impurities away from the well confined region into the isolation chamber. In the divertor chamber, D^+ and impurity ions are removed from the system with cryogenic pumps. Since impurities are relatively good radiators, the energy conducted and/or convected into the divertor is converted to line radiation and uniformly distributed on the divertor walls where it can be removed.

Realistic poloidal divertor geometries have taken several forms over the last fifteen years. Initially, closed divertor designs with both upper and lower chambers, such as in the ASDEX tokamak, were used. High confinement H–modes were originally obtained with closed divertors in ASDEX (3). One serious drawback of the closed divertor design is a severely reduced ability to shape the well confined plasma volume and to control the SOL geometry. A second generation of poloidal divertors used an open chamber design which allowed much more shaping flexibility. Tokamaks such as DIII–D and JET have successfully used the open divertor approach to produce record core plasma pressure and confinement levels. Recently, with the addition of cryogenic pumping systems, baffles, contoured graphite divertor surfaces and well controlled distributed gas puffing systems, open divertors have substantially exceeded the performance levels attained with closed divertors.

The basic elements of an open axisymmetric poloidal divertor are shown in Fig. 1. The white region in the figure shows where the well confined main plasma resides in a typical H–mode discharge. The shaded region is located outside the 98% flux surface. It covers the boundary layer, the separatrix and the SOL out to the vacuum vessel walls. The separatrix nominally divides the inner, closed field line region, from the outer open field line region. The detailed wall geometry, as well as the material used for plasma facing surfaces, vary from one tokamak to another. Figure 1 shows the

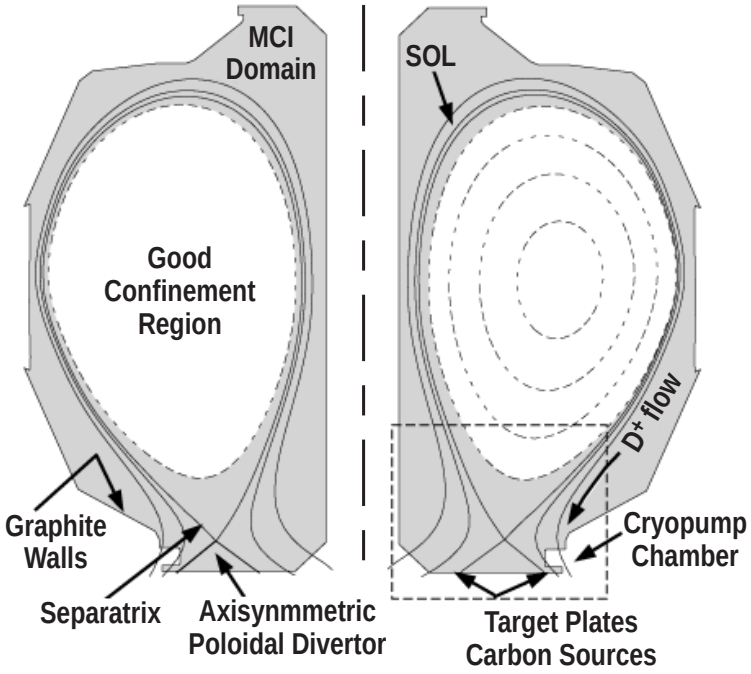

FIGURE 1. Poloidal cross section of a lower single-null DIII–D configuration. The principal components needed to understand the operation of axisymmetric divertors are illustrated. The shaded area indicates the typical edge transport modeling domain with the MCI code.

wall geometry for DIII–D in a lower single null divertor configuration. With the exception of a few specialized components such as rf antennas, all of the DIII–D plasma facing surfaces are covered with graphite.

The primary goal of the divertor is to compress impurity ions and helium produced during DT fusion reactions into a region as close as possible to the target plates. Ideally, drag from the D^+ flow along with parallel electric fields in the SOL provide the compressive forces for this process. These forces are nominally directed toward the target plates while thermal gradient forces acting on impurity ions typically oppose the compressive forces and act to pull impurities back up the SOL field lines toward the mid-plane region where they can easily be transported into the main plasma. Unfortunately, the nominal picture of the compressive forces is not always applicable to fusion relevant divertor operations and the dynamics of scrape-off layer flows are more complex than the simple picture envisioned above. In fact, it is now known that in tokamaks sometimes conditions in isolated areas of the SOL are such that the D^+ flows reverse direction and actually assists the thermal gradient forces in pulling impurities out of the divertor region. The physics involved in the onset of these flow reversal regions and the detailed 2D structure of the flow patterns are known to be sensitive to impurity cooling rates and thus to the production and transport of impurities ions from each of the plasma facing material surfaces.

Recently, new diagnostics which measure the parallel D^+ and carbon impurity ion flows in the DIII–D divertor have acquired data which may give us a better understanding of how to modify or control their properties. Techniques such as heavy

deuterium gas puffing in the SOL to increase the D^+ flow have been effective in substantially reducing the electron temperature (T_e) and increasing the density (n_e) in the divertor while increasing the radiated power near the target plates. Substantial differences in the flow patterns are observed after injecting large deuterium gas puffs into the SOL. Impurity gas puffs, using species such as neon, argon and nitrogen, have also been used to increase the divertor radiation. This approach sometimes results in higher core plasma Z_{eff} values but may, if properly designed and controlled, ultimately lead to better control of divertor flows and atomic processes which influence other aspects of the divertor performance. These so-called radiative divertor approaches using either D_2 puffing alone or combination of D_2 and impurity puffs are currently an active area of research in diverted tokamaks.

In principle, a pure D_2 radiative divertor is particularly promising if T_e near the target plates can be driven low enough (~1 eV) to obtain a fully recombining divertor plasma without disrupting the main plasma. This scenario is especially attractive because it avoids difficulties with non-intrinsic impurity puffs which can result in a core plasma with Z_{eff} above 1.6. A fully recombining D_2 radiative divertor also reduces intrinsic carbon impurities from physical sputtering and theoretically leads to a reduction in the thermally activated contribution of the chemical sputtering at the target plates. On the other hand, the recombining divertor approach is more difficult with advanced tokamak confinement scenarios where current and pressure profile control, critical for maintaining stability, requires low density/high temperature operation.

Thus, the next major step in the development of tokamaks and generally in the advancement of fusion energy research hinges on our ability to control the boundary layer, SOL, and divertor without impinging on the shaping flexibility needed to maintain high core confinement levels with good stability properties. This is a sizable challenge requiring creative new ideas, advanced hardware concepts, and a substantial theoretical and modeling commitment which must be benchmarked against a continuing stream of experimental data from our existing machines. Since atomic and molecular physics is a keystone in the dynamics of a fusion plasma's boundary, increasing demands are being put on the quality, accuracy, and extent of the atomic data used as well as our ability to produce and benchmark this data. The objective here is to highlight the role of atomic physics in divertor modeling and point out what types of data are needed for developing a better understanding of the complex processes found at the edge of a fusion plasma.

III. MCI MODELING APPROACH

The basic transport physics used in edge plasma fluid and Monte Carlo codes is essentially identical. Single and multi-species fluid codes are primarily used in collisionally dominated regions of the edge plasma while Monte Carlo codes are required in regions with large gradients or when the mean free path of a particular ion species is long compared to the local geometric scale, for example near plasma facing

surfaces or in regions of low collisionality. A general review of edge plasma fluid and Monte Carlo codes can be found in a paper by Stangeby (4).

The current generation of Monte Carlo impurity codes are quasi-kinetic in the sense that they do not fully account for drift kinetic or velocity space diffusion effects such as is done in a Fokker-Planck code. A full Fokker-Planck treatment of the impurities would be computationally prohibitive with today's CPUs. The general approach used in Monte Carlo impurity codes is to follow an individual "particle" through a computational domain in which the background plasma parameters change as a function of space but are fixed in time. The computational domain for the DIII–D MCI code is depicted by the shaded region in Fig. 1. It extends from the vessel walls into the edge of the well confined plasma just inside the separatrix. A simulation "particle," which starts as neutral atom or molecule from a plasma facing surface, moves from one cell on a grid to a neighboring cell and interacts with the background plasma in each cell on the grid.

The trajectory of a "particle" is determined from the three-vector force components acting on it at each position in the cell. In addition, the properties of the "particle," such as its charge state, temperature, and flow velocity are tracked and stored for additional statistical analyses. As the simulation evolves, spatial and temporal histories of the "particles" are used to calculate spatial density distributions and average residence times in the plasma. In order to obtain reasonable simulation times for individual code runs, each "particle" actually represents a specified number of impurity atoms or molecules. This approach provides an accurate description of the impurity distribution as long as a statistically significant number of "particle" histories are tracked for each simulation.

A. Transport Physics

In the MCI code, impurity ion transport is driven by both kinetic and collective effects such as: collisional diffusion, electric field drifts, drag from flows in the background ions, and thermal gradient forces due to the background ions and electrons. Kinematically, impurity ions undergo a classical guiding center motion along the magnetic lines of force *i.e.*, parallel motion and an anomalous motion normal to the magnetic field due to turbulent transport processes *i.e.*, perpendicular motion.

The first step in the transport process is to calculate a characteristic time interval, $\Delta t'$, in each cell. $\Delta t'$ is determined by the local electron-ion collision time. An internal transport time interval Δt is then chosen such that $\Delta t = \min(\Delta t_b, 0.02\Delta t')$. $\Delta t_b = s_{pol}|v_{\|Tz}|^{-1}$ is the time required to reach either a cell boundary or material surface, where $|v_{\|Tz}| = (kT_z/m_z)^{1/2}$ is magnitude of the impurity ion thermal velocity. $s_{pol} = s_{\|}\sin\zeta$ is the poloidally projected distance along the field line, k is the Boltzmann constant, m_z is the mass of the impurity ion, T_z is the temperature of the impurity ion, ζ is the angle the magnetic field line makes with a unit vector in the toroidal direction and $s_{\|}$ is the parallel distance to the cell boundary or a material surface.

Once the internal time step has been established a new spatial position along the field line ($s_{||,i+1}$) is calculated based on the current position ($s_{||,i}$) and the current parallel flow velocity ($v_{||,i}$) of the impurity ions using the following expression:

$$s_{||,i+1} = s_{||,i} + v_{||,i}\Delta t + \frac{1}{2}C_i(\Delta t)^2 + \gamma_{rs}\sqrt{2D_{||,i}\Delta t} \tag{1}$$

The acceleration coefficient C_i is given by:

$$C_i = \frac{v_b - v_{||,i}}{\tau_{sl}} + \frac{1}{m_z}\left[0.71Z_z^2\frac{\partial T_e}{\partial s_{||}} + \beta_z\frac{\partial T_b}{\partial s_{||}}\right] + \frac{Z_z eE}{m_z} \tag{2}$$

In Eq. (2) v_b and T_b are the background deuterium ion D^+ parallel flow velocity and temperature respectively, Z_z is the charge of the impurity ion, E is the parallel electric field, e is charge of an electron, τ_{sl} is the impurity ion collision time with the background ions given as:

$$\tau_{sl} = \frac{m_z T_b\sqrt{\left(T_b/m_b\right)}}{6.8\times10^4 Z_z^2 Z_b^2 n_b \ln(\Lambda)\left[1+m_b/m_z\right]} \tag{3}$$

and β_z is the ion thermal gradient coefficient (5) given by:

$$\beta_z = \frac{3\left[\mu + 7.07Z_z^2\left(1.1\mu^{5/2} - 0.35\mu^{3/2}\right) - 1\right]}{5.4\mu^2 - 2\mu + 2.6};\mu = \frac{m_z}{m_b + m_z} \tag{4}$$

In Eq. (3) $\ln(\Lambda)$ is the Coulomb logarithm which typically ranges between 10 and 20 for cases of interest while n_b, Z_b, and m_b are the density, charge, and mass of the background ions respectively. The fourth term on the right hand side of Eq. (1) accounts for the classical diffusion of impurity ions along the magnetic field lines due to collisions between the impurity ions and the background ions. The coefficient γ_{rs} is a random sign operator which, on average, switches only once between positive and negative during each ion-ion collisional time *i.e.*, approximately every 50 $\Delta t'$ internal time steps based on the constraint $\Delta t = \min(\Delta t_b, 0.02\Delta t')$. The classical parallel diffusion coefficient $D_{||,i}$ in Eq. (1) is calculated with the current impurity ion temperature $T_{z,i}$ and the parallel impurity ion collision time $\tau_{||,i}$ using the following expression:

$$D_{||,i} = 1.22\times10^8\left(\frac{\tau_{||,i}T_{z,i}}{m_z}\right) \tag{5}$$

where $\tau_{\|,i}$ is given by:

$$\tau_{\|,i} = \frac{m_z T_{z,i} \sqrt{\left(T_b / m_b\right)}}{6.8 \times 10^4 Z_z^2 Z_b^2 n_b \ln(\Lambda)} \tag{6}$$

In addition to calculating the new parallel spatial position $s_{\|,i+1}$, a new impurity ion temperature $T_{z,i+1}$:

$$T_{z,i+1} = T_{z,i} + \left(T_b - T_{z,i}\right)\frac{\Delta t}{\tau_{se}} \tag{7}$$

and flow velocity $v_{\|,i+1}$:

$$v_{\|,i+1} = v_{\|,i} + C_i \Delta t \tag{8}$$

are obtained after each internal time step. In Eq. (7) τ_{se}, the collisional Spitzer energy transfer time, is given by:

$$\tau_{se} = \frac{m_z T_b \sqrt{\left(T_b / m_b\right)}}{1.4 \times 10^5 Z_z^2 Z_b^2 n_b \ln(\Lambda)} \tag{9}$$

and C_i is the acceleration coefficient given by Eq. (2). The spatial-diffusion approach used to simulate impurity pressure gradient driven motion parallel to the field lines, as specified by $D_{\|,i}$ in Eqn. (5), is not satisfactory in all situations encountered. Thus, a velocity-diffusion model is currently under development which can be compared with the approach outlined above.

Perpendicular transport is modeled with an anomalous cross-field diffusion coefficient, $D_\perp$, using a random Monte Carlo algorithm similar to that of parallel diffusion. In terms of the cross-field variable x_i the new perpendicular position x_{i+1} of an impurity ion after each internal time step is given by:

$$x_{i+1} = x_i + \gamma_{rs}^* \sqrt{2 D_\perp \Delta t} + v_{pinch} \tag{10}$$

Since we lack an experimentally verifiable theory of anomalous cross-field diffusion in the SOL and divertor, MCI uses a semiempirical value for $D_\perp$ along with a constant pinch velocity v_{pinch}. The values of $D_\perp$ used matches those obtained in edge transport codes when reproducing experimentally measured radial density profiles. This value typically ranges between $0.1 \le D_\perp \le 1.0$ m^2/s for most DIII–D plasmas.

B. Intrinsic Versus Non-Intrinsic Impurities and Nonlinear Effects

MCI is used to simulate both intrinsic and non-intrinsic impurities. In DIII–D and other tokamaks non-intrinsic gas puffs, with impurities such as neon, argon, and nitrogen, are frequently used either for diagnostic purposes or for radiative divertor experiments. Thus, it is of considerable interest to model the transport of these impurities along with the intrinsic impurities. On the other hand, prior to performing simulation of non-intrinsic impurities, it is necessary to understand the sputtering, transport and radiation physics of the intrinsic impurities in the discharge of interest. This is particularly important because, in many cases, radiative cooling by the intrinsic impurities is known to produce substantive changes in the properties of the background plasma which then affect the transport of the non-intrinsic impurities. The question of how to feed back radiative cooling effects on the background plasma is a central issue for divertor modeling codes. This is presently beyond the scope of all the existing Monte Carlo models due to the intrinsically nonlinear, time dependent, nature of the problem. Nevertheless, a concerted effort is being made to address this issue since virtually all of the important mechanisms involved in establishing how the divertor performs when approaching fusion relevant conditions, such as detachment and flow reversal, depend on the nature of cooling processes.

Since essentially all of the DIII–D plasma facing material is graphite, the primary intrinsic impurity tracked in MCI is carbon. In this paper we limit our discussion to the linear modeling of intrinsic carbon in DIII–D.

C. Neutral Sources, Atomic Data, and Computational Grids

Neutral carbon "particles" are sputtered from plasma facing surfaces with a Thompson energy distribution (6) which depends on the energy of the incident ion or neutral. The sputtered neutral atoms and molecules follow straight line trajectories, based on their launch angle and energy, until they are ionized by collisions with the background plasma. Ionization mean free paths of carbon atoms depend on their launch angle, energy, and the plasma density and temperature at the location of the sputtering site.

In MCI, the entire plasma facing surface is divided into small segments where the surface properties are individually specified according to known or experimentally measured conditions and sputtering yields are calculated with a variety of semiempirical and physics based models. These models are driven by background plasma ion and neutral fluxes impinging on each segment and by carbon ions and neutrals which have been transport across the plasma after being produced at the same or other wall segments (*i.e.*, self-sputtering events). Two basic types of sputtering models are used in MCI, physical and chemical sputtering. Currently, MCI has four options for physical sputtering and one for chemical sputtering. In addition, the chemical sputtering model is driven by a physical sputtering process so any of the four physical sputtering processes can be used in chemical sputtering model. Each of the physical sputtering models account for electrostatic sheath effects, the Maxwell-

Boltzmann properties of the incident flux, and threshold energy effects while the chemical sputtering model has an explicit dependence on the local surface temperature which can, in some cases, be experimentally measured with an infrared camera. Thus, MCI has a complete set of erosion and redeposition models which are coupled to a realistic divertor and core plasma. As comparisons are made with experimentally measured erosion and redeposition profiles we are learning which of the various models best fit a particular set of experimental conditions and are able to identify additional physics constraints which need to be included in the models.

The current version of the MCI chemical sputtering model is based on the Roth García-Rosales (7) approach. This model only describes the production of methane (CD_4) and does not address processes associated with the release of heavier hydrocarbons in the C_2D_x and C_3D_x complex. There is experimental evidence indicating these larger hydrocarbon chains (8,9) may also be important in low temperature divertors but as yet we do not have access to good models for these sputtering processes.

During the transport process, collisions between the background plasma particles and impurity ions, neutral atoms or neutral molecules can result in a change in the impurity's charge state. As seen from the transport equations, the parallel forces on the impurity ions have a quadratic dependence on the charge state. After each simulation step Δt a series of Monte Carlo tests are made using tabulated atomic rates from the ADPAK database. During these tests, MCI calculates the probability of a change in the charge state due to an ionization, recombination or neutral charge exchange event and adjusts the transport accordingly. Thus, the accuracy of the atomic data can have a substantial impact on the simulation results. The ADPAK database uses a compilation of experimental and theoretical rates. Polynomial fits to the data are used to estimate ionization, recombination, charge exchange and radiation rates as needed for various background plasma condition. The ADPAK database is now about 15 years old.

The local electron temperature is used when calculating atomic rates with ADPAK data. In MCI, this temperature is obtained, along with the other background plasma properties such as the ion density and temperature, from the UEDGE (10) fluid code. Relatively small changes in the electron temperature can have a measurable impact on the impurity ion transport through the strong charge dependence. The electron temperature also plays a key role in the line emission rates which are used to calculate 2D radiation patterns that are compared to experimental measurements and to make quantitative predictions of the total radiated power and cooling rates. Thus, the accuracy of the electron temperature in each cell on the simulation grid is critical for the success of the simulation results. If the cells on the simulation grid are too large compared to the gradient scale lengths established by the plasma, then the discreteness of the background plasma temperature artificially skews the transport and line emission modeling in the MCI code.

MCI is unique compared to other Monte Carlo impurity codes such as DIVIMP (11) in that it has its own internal grid generator. The grid is constructed from an unstructured mesh making it possible to simulate practically any geometric boundary

shape. The MCI grid generator is also used to identically reproduce the UEDGE grid and extend it out to the vessel walls. Figure 2 shows the lower divertor region, as references by the dashed rectangular outline in Fig. 1, for two of the grids available in MCI. An unextended UEDGE grid is shown on the left and the corresponding standard MCI grid for the same plasma equilibrium is shown on the right. MCI simulations may be run on either grid or on a nonorthogonal UEDGE grid extended to the walls with an orthogonal MCI grid. Note that the resolution of standard MCI grid is higher than that of the standard UEDGE grid and may be increased of decreased to better match the experimental measurements. Computational time is only moderately increased with grid density in MCI.

IV. DISCUSSION AND MCI RESULTS

MCI is presently being used primarily as an interpretive tool for better understanding the dominant physical processes controlling the divertor performance. Over the course of its development the code has been tested and benchmarked against both fluid and Monte Carlo codes as well as against a variety of experimental data. These benchmarks have been used to identify weak points in the MCI modeling approach and to improve the underlying physics models used by the code. In the following discussion we will highlight some of the results from these benchmarks and summarize the conclusions drawn from them.

A. Comparisons with Other Codes

The standard simulation approach used in MCI involves detailed source modeling and realistic wall conditions as outlined in the previous section. It is also possible to reproduce the boundary conditions used in the UEDGE code and to compare the carbon transport results obtained with each of these codes. This comparison was done

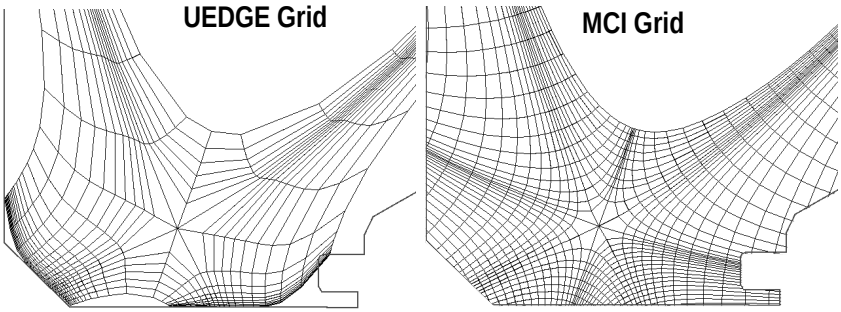

FIGURE 2. Comparison of two grid options which are possible with the MCI grid generator. The low resolution grid on the left is the standard UEDGE grid and the high resolution grid on the right is the standard MCI grid. The standard UEDGE grid can also be extended out to the walls with the MCI grid generator.

for a case in which the divertor plasma was attached to the outer target plate and detached from the inner target plate. These plasmas are typically more straightforward to model because they are less likely to be dominated by nonlinear processes. Several of the changes which had to be implemented in order to reproduce the UEDGE boundary conditions were: the use of a constant sputtering yield, $Y = 10^{-3}$, on each plasma facing surface segment and a modification of the way in which the carbon neutrals are launched from the surface segments. A 2D cosine launch distribution was used and the launch energy was set to match that of the deuterium ions in the cells intersecting the wall segment where a neutral is launched. The edge of the standard UEDGE grid, as shown on the left in Fig. 2, became the plasma facing surface rather then the vessel walls. The sputtering probability along the bottom of the UEDGE grid for this case is shown in Fig. 3.

The integrated source rate and distribution for the two codes, as shown in the figure, is 31.6 Amps of neutral carbon current. UEDGE simulation resulted in a total carbon content, integrated over all charge states, of 1.11×10^{18} particles. This is all the carbon accumulated in the computational domain once a steady state has been reached. It does not include carbon in the well confined plasma volume. The MCI simulation resulted in less carbon by about a factor of 2.6 *i.e.*, a total content of 3.04×10^{17} carbon particles. The largest discrepancy between the two codes is in the total number of C^{2+} ions. The UEDGE simulation yields about 12 times more C^{2+} than MCI. On the other hand, UEDGE and MCI agree relatively well in their C^{5+} and C^{6+} content. MCI and DIVIMP have also been compared using the same data as for the UEDGE comparison. The two Monte Carlo codes agree in total carbon content to within a few percent (12). Based on a series of sensitivity studies done with MCI, as described in the next section, some of the differences between the two codes appear to be related to small variations in the atomic data used. UEDGE and MCI utilized slightly different versions (different internal database switch settings) of ADPAK data for these comparisons. Direct cell-to-cell comparisons of the atomic data are underway to resolve these differences. UEDGE also includes elastic carbon-deuterium neutral collisions in its calculation of the neutral carbon transport. This option is currently being implemented in MCI.

B. The Effects of Atomic Data on Carbon Transport

MCI is used to assess how uncertainties in atomic data affect impurity ion transport and radiation physics. Uncertainties in atomic data can have a relatively large impact on simulation results when parts of the divertor plasma are entering a nonlinear regime. This is typically the case during strongly driven target plate detachment processes or during the formation of a high density, highly radiating, cold plasma (MARFE) (13) near the divertor X–point. We see from Eqs. (2) and (3) that the background ion temperature plays an important role in both the drag term, with a

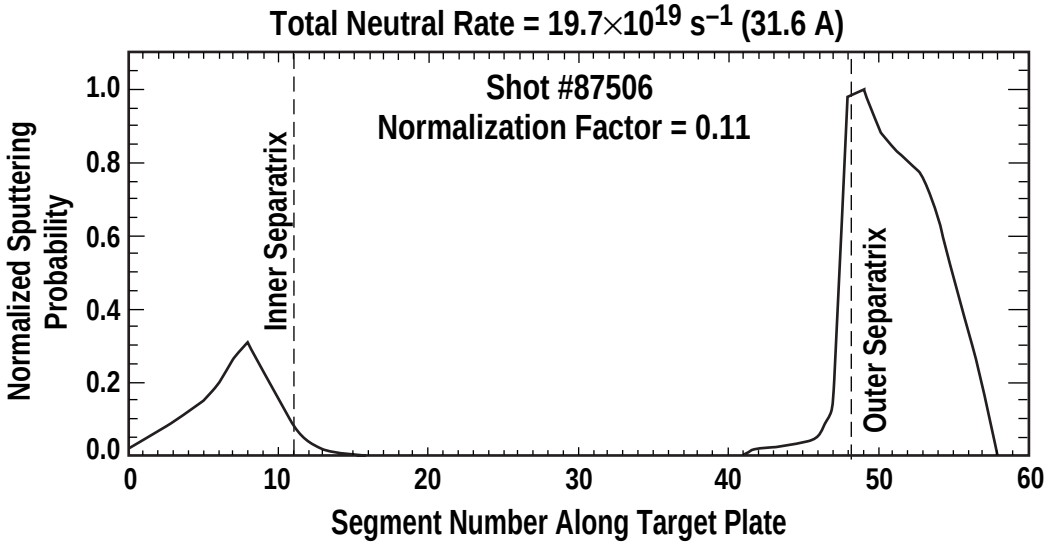

FIGURE 3. Normalized carbon sputtering probability along the lower boundary of the UEDGE grid shown in Fig. 2 for a constant Y = 10^{-3} sputtering yield.

$T_b^{-3/2}$ dependence, and in the ion thermal gradient term when regions of high radiation are present in the divertor. This changes the impurity transport and thus the availability of impurities for assisting in the local cooling of the background plasma. In this section we briefly describe the results of a series of test which were done on the C^0, C^+, D^0, and D^+ charge exchange rate.

For this comparison we increased the charge exchange rate of $C^+ + D^0 \rightarrow D^+ + C^0$ from essentially zero in each cell to a rate equivalent to that for the $C^0 + D^+ \rightarrow D^0 + C^+$ charge exchange process. With the same parameters as used for the comparison discussed in the previous section, this corresponded to a $\langle\sigma v\rangle_{cx}$ of 2.45×10^{-9} $cm^3 s^{-1}$ in the cells just above wall segments 4 → 12, as shown in Fig. 3, where T_e = 1.5 eV. With both change exchange processes, the integrated carbon sputtering source rate increased from 31.6 to 38.6 Amps while the total UEDGE carbon inventory decreased from 1.11×10^{18} to 6.23×10^{17} particles and MCI's total carbon inventory decreased from 3.04×10^{17} to 2.24×10^{17} particles. In addition, the average lifetime of the carbon particles decreases from 1.55 to 0.93 ms in the MCI simulations. It is interesting to note that in the case with only the energetically allowed $C^0 + D^+ \rightarrow D^0 + C^+$ charge exchange process the total carbon content increased even though there was a smaller sputtering source rate. In this case, MCI estimates of the total power radiated by the carbon in the divertor increased to approximately 46.7 kW whereas with both charge exchange processes the carbon radiation in the divertor was 37 kW. While this radiated power level is still considerably lower than the 382 kW estimated from bolometer measurements it does produce a modest improvement in the radiated power by increasing the total carbon inventory.

An impurity ion tracking algorithm was developed for the MCI code to facilitate studies of how the various terms in the transport equations given above affect the trajectories of impurities as they move through the computational domain. The

histories of individual impurity ions are recorded during a simulation and played back in slow motion. As the impurity moves from one time step to another and from cell to cell, the current charge state is displayed and statistics are gathered about the probability of an impurity in a particular charge states escaping from the divertor along with details about the motion of the impurities in various regions of the plasma. In a plasma with a attached outer separatrix, a majority of the carbon impurities are generated near the region where the outer separatrix intersects the divertor target plate *i.e.*, the outer strike point as shown in Fig 3. Thus we are primarily interested in the dynamics of these particles.

Studies of the most statistically significant transport pathways for carbon originating from the outer strike point indicate that C^+ ions created very near the outer strike point target plate have a relatively high probability of escaping the divertor compared to the other transport pathways available. Since the recombination rate in this region is orders of magnitude lower than the ionization rate to the C^{2+} charge state, we find a high probability for $C^+ \rightarrow C^{2+}$ in the first few cells above the target plate. In both charge states, the dynamical balance between the drag due to the deuterium ion flow and the ion thermal gradient force is relatively well maintained. On the other hand, the C^+ ions are relatively cold compared to the background ions in these cells *i.e.*, their thermalization time is long compared to their residence time. Once they become C^{2+} ions their thermalization time is reduced by a factor of four and their parallel diffusion rate increases accordingly. The tracking results clearly show that the escape probability increases with the charge of the impurity ion and reaches approximately 50% in the C^{3+} charge state.

Thus, we see from the discussions of the forces on the C^+ ions given above that the artificial inclusion of an enhanced $C^+ + D^0 \rightarrow C^0 + D^+$ charge exchange rate can be expected to result in a reduction of the carbon inventory in the plasma because it removes C^+ ions from the cells near the targets. This effectively lowers the escape probability of the carbon from the divertor. Thus, as noted above the carbon inventory was reduced when the $C^+ + D^0 \rightarrow C^0 + D^+$ process was included.

Once a carbon ion escapes the divertor region it either goes into the well confined plasma or travels over the top of the discharge, along the inner wall, and down to the inner strike point region. Since the inner strike point is typically detached and the plasma is relatively cold in this region the recombination rate becomes significant compared to the ionization rate and most of the carbon ions are neutralized. The carbon neutrals tend to build up near the inner wall but can also re-ionize and move back up an outer SOL flux tube. A majority of these second generation ions get transported into flux tubes where the flow toward the inner strike plate once again dominates the force balance and eventual re-enter the high recombination zone. Thus, the dynamics in the inner SOL region form a kind of closed loop which results in a build up of the local carbon density. This build up is typically seen in the C^{2+} emissions from the region as shown in the next section.

C. Benchmarks on Experimentally Measured CIII Images

An example of how MCI simulations are benchmarked against experimental data is shown in Fig. 4. An experimentally measured 2D distribution of the C^{2+}, λ = 465 nm, line emission is shown in the upper part of the figure and the calculated emission pattern, using the carbon source from Fig. 3, is given in the lower part of the figure. Reasonably good qualitative agreements are found in regions with high emission rates. As mentioned in Section B above, an estimate of the total power radiated by the carbon for this case is about a factor of ten below that implied by bolometer measurements of the region suggesting that the simulated carbon content is too low.

D. Comparison of Physical and Chemical Sputtering

Detailed comparisons between the case discussed above *i.e*, Y = 10^{-3} physical sputtering only and simulations with both physical and chemical sputtering have been described in a previous paper (14). Here we briefly summarize the key results. The

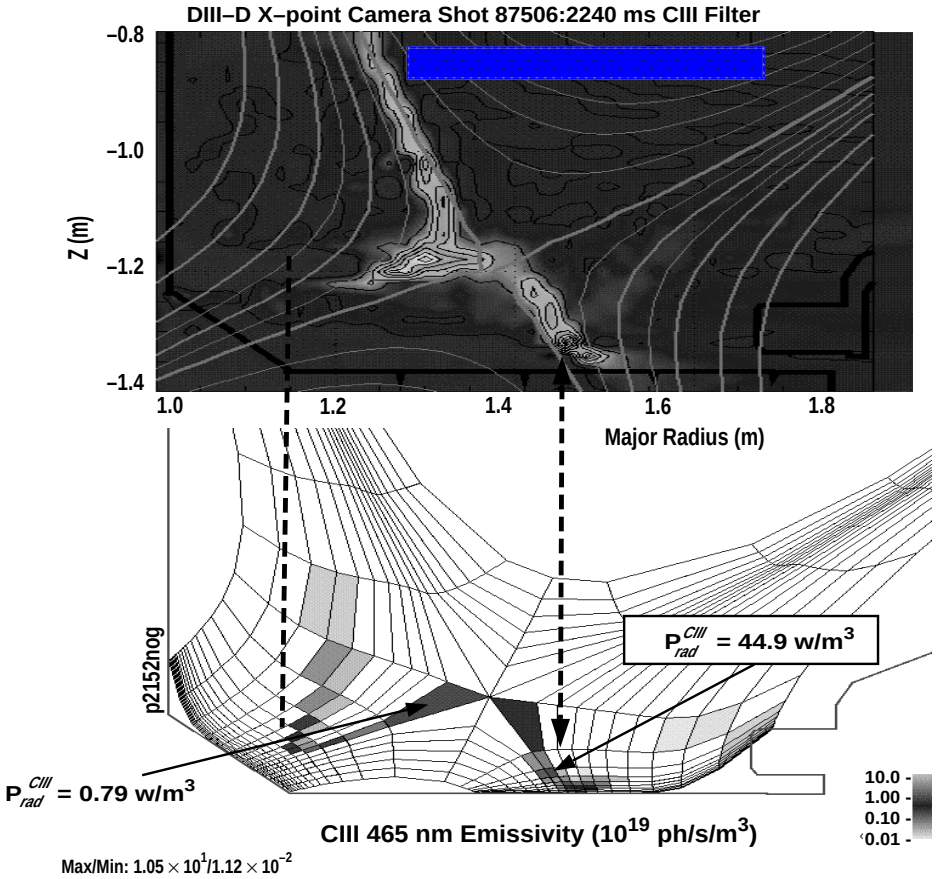

FIGURE 4. Comparison of the measured C^{2+} emissions (above) and those calculated with MCI (below) for shot 87506.

source distribution for the combined sputtering case was similar to that shown in Fig. 3 but the integrated neutral carbon source rate increased from 1.97×10^{20} s^{-1} without chemical sputtering to 1.70×10^{21} s^{-1} with chemical sputtering. While the total carbon inventor increased to 6.11×10^{17} particles with chemical sputtering there was essentially no increase in the neutral carbon inventory. In fact, the C^{+} content doubled while the C^{2+} and C^{3+} content went up by a factor 4 to 5. As a result, the power radiated from the carbon in the divertor, as estimated from the MCI simulation, increased to approximately 165 kW or roughly half that measured with the bolometer.

V. SUMMARY AND CONCLUSIONS

An overview of the MCI model has been presented along with a representative summary of recent results. MCI simulations are in reasonably good agreement with other fluid and Monte Carlo impurity codes and with experimental measurements in DIII–D. Simulated 2D carbon line radiation patterns agree qualitatively with line filtered images of the C^{2+} emission patterns observed in the DIII–D divertor and total radiated power measurements agree to within a factor of two with those calculated in MCI. The next step required to improve MCI's results is to address the role of nonlinear effects in the simulations. Improvements in the accuracy of the atomic data are essential for simulating nonlinear effects.

ACKNOWLEDGMENT

Work supported by U.S. Department of Energy under Contract No. DE-AC03-89ER51114. Valuable comments by G.D. Porter and W.P. West on comparisons between MCI and UEDGE are gratefully acknowledged. We would also like to thank P. C. Stangeby for suggestions on comments on comparisons with DIVIMP.

REFERENCES

1. Janeschitz, G., Plasma Phys. Contrl. Fusion **37** (1995) A19.
2. Keilhacker, M., *et al.*, Plasma Phys. Contrl. Fusion **37** (1995) A3.
3. Wagner, F., *et al.*, Phys. Rev. Lett. **49** (1982) 1408.
4. Stangeby, P.C., Contrib. Plasma Phys. **28** (1988) 507.
5. Neuhauser, J., et al., Nucl. Fusion **24** (1984) 39.
6. Thompson, M.W., Philos. Mag., **18** (1968) 377.
7. Roth, J., and García-Rosales, C., Nucl. Fusion **36** (1996) 1647, and Corrigendum, Nucl. Fusion **37** (1997) 897.
8. Haasz, A.A., Davis, J.W., J. Nucl. Mater. **175** (1990) 84.
9. Yamada, R.J., J. Nucl. Mater. **174** (1990) 118.
10. Rognlien, T.D. *et al.*, J. Nucl. Mater. **196-198** (1992) 347.
11. Stangeby, P.C., and Elder, J.D., J. Nucl. Mater. **196-198** (1992) 258.
12. Stangeby, P.C., personal communication (1997).
13. Petrie, T.W., *et al.*, Nucl. Fusion **37** (1997) 643.
14. Evans, T.E., *et al.*, Contrib. Plasma Phys. **38** (1998) 260.